Tunable magnetic and optical properties of transition metal dihalides by cation alloying

Mark Blei, Jesse Kapeghian, Rounak Banerjee, Pranvera Kolari, Blake Povilus, Yashika Attarde, Antia S. Botana, and Sefaattin Tongay

Phys. Rev. Materials **6**, 084003 — Published 11 August 2022

DOI: 10.1103/PhysRevMaterials.6.084003

Tunable Magnetic and Optical Properties of Transition Metal Dihalides by Cation Alloying

Mark Blei[1,†], Jesse Kapeghian[2,†], Rounak Banerjee[1], Pranvera Kolari[1], Blake Povilus[1], Yashika Attarde[1], Antia S. Botana[2*], and Sefaattin Tongay[1*]

[1] Materials Science and Engineering, School for Engineering of Matter, Transport and Energy, Arizona State University, Tempe, AZ 85287, USA
[2] Department of Physics, Arizona State University, Tempe, AZ 85287, USA
[†] Both authors contributed equally.
* Corresponding author Sefaattin.tongay@asu.edu and Antia.Botana@asu.edu

Abstract

Alloying has been a tradition in materials science that has enabled groundbreaking discoveries in semiconductor technologies, optics, and photovoltaics, among others. While alloying in traditional systems is relatively well-established, the effects of alloying in the newly emerging van der Waals (vdW) two-dimensional (2D) magnets are still in their infancy. Using $Co_{1-x}Ni_xCl_2$ as a testbed system, our results show that chemical vapor transport of stoichiometric mixtures of $TeCl_4$, Co, and Ni enables the synthesis of highly crystalline vdW magnetic alloys with excellent control over the Ni concentration (x) without any tellurium impurities or phase separation. The method is advantageous compared to binary $CoCl_2$ and $NiCl_2$ precursor mixtures which only produce small-sized crystals with a large compositional variation. Magnetic measurements show that the degree of magnetic anisotropy, Weiss temperature, and Néel temperature (T_N) strongly correlate to the Ni concentration, offering a tune-knob to engineer the magnetic behavior of transition metal dihalides. First-principles calculations offer further insights into how the increasing Ni content influences the inter- and intra-layer magnetic couplings and the resulting magnetic response. Overall, our findings provide an important avenue towards metal cation alloying in dihalide 2D vdW magnets and offer new means to tune their magnetic behavior on demand.

Introduction

The experimental discovery of two-dimensional (2D) magnetic ordering at the mono- and few-layer limit in $FePS_3$ [1], CrI_3 [2], $CrCl_3$ [3], $Cr_2Ge_2Te_6$ [4], and Fe_3GeTe_2 [5] has stimulated intense research activities. In particular, transition metal trihalides (MX_3, M=transition metal, X=halogen) have attracted a lot of attention [4,6-13] with active efforts directed at tuning their magnetic response on demand by external means. Recent studies [14,15] have shown that the electric, optical, and magnetic properties of Cr-trihalides can actually be tuned by intermixing the halide anions in ternary $CrI_{3-x}Br_x$ [15] or quaternary $CrCl_{3-x-y}Br_xI_y$ [16] systems.

While much attention has been paid to trihalides, a related family of materials, transition metal dihalides (MX_2), has recently emerged as the focus of interest in the context of 2D magnetism [6,7,17,18]. One significant difference between these two families is that whereas trihalides display an underlying honeycomb lattice for their magnetic ions, in dihalides a triangular lattice is present instead. Two relevant members of the transition metal dihalide family are $CoCl_2$ and $NiCl_2$, both of which have $CdCl_2$ trigonal crystal structures (space group, $R\bar{3}m$) [19-21], as shown in **Fig. 1a**. Below their ordering temperatures (25 K and 52 K for the Co and Ni materials, respectively) both of these compounds adopt a magnetic structure consisting of ferromagnetic layers (with in-plane moments) coupled antiferromagnetically out-of-plane [21-24]. Neutron diffraction results indicate that both $CoCl_2$ (with a Co^{2+}: $3d^7$ electronic configuration) and $NiCl_2$ (with Ni^{2+}: $3d^8$) favor high-spin states, with $S = 3/2$ for Co, and $S = 1$ for Ni.

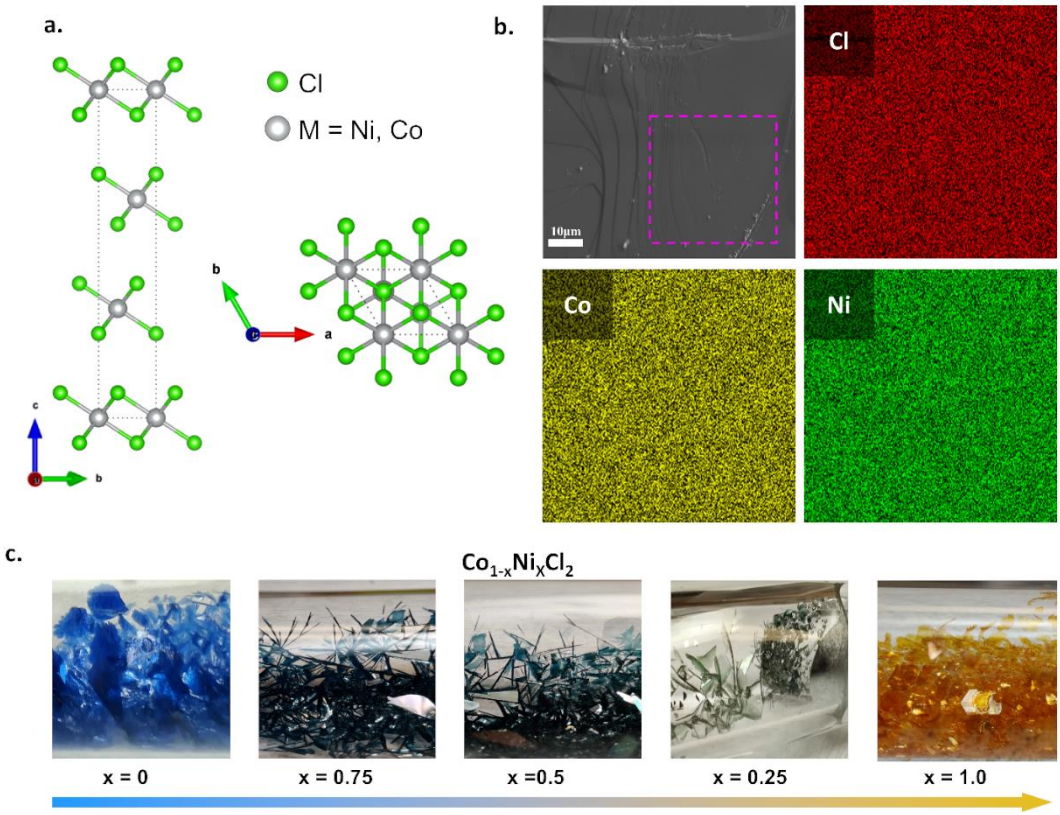

Figure 1: (**a**) Crystal structure of transition metal (M) dihalides $CoCl_2$ and $NiCl_2$ from side and top views. M atoms are shown as gray spheres, Cl atoms are shown as green spheres, and the unit cell is indicated by a dotted line. (**b**) SEM/EDS images and mapping of $Co_{1-x}Ni_xCl_2$, where $x = 0.25$. (**c**) Optical images of cobalt-nickel dihalides as the Ni composition (x) increases from 0 to 1. Further experimental details can be found in Appendix A-C.

In this work, we show how cation alloying in vdW transition metal dihalide magnets can be used to engineer the electronic structure and magnetic properties of these materials. The $Co_{1-x}Ni_xCl_2$ ($0 < x < 1$) ternary alloys were synthesized through chemical vapor transport (CVT) growth. Comprehensive Raman spectroscopy, energy-dispersive X-ray spectroscopy (EDS), and x-ray diffraction (XRD) studies show the synthesized crystals are highly crystalline and are fully alloyed without any phase separation. Further, vibrating sample magnetometry (VSM) was employed to probe the magnetic properties of these materials across the compositional spectrum. Combining our experimental findings with first-principles calculations, our study offers the first insights on how engineering the electronic environment in $Co_{1-x}Ni_xCl_2$ as a function of x influences the magnetic response of these materials.

Results

Previously, transition-metal dihalide crystals were synthesized in their binary form (such as $CoCl_2$ and $NiCl_2$) using a self-flux technique and chemical vapor transport [25]. However, their alloys, whether in halide anion or metal cation form, have not been realized. The question arises if Co and Ni metal cations could be intermixed with each other in a predictable and controllable way across the ternary phase diagram. If possible, this would enable us to potentially engineer the magnetic response of the material including its Néel Temperature (T_N), magnetic susceptibility

(χ_m), and magnetic anisotropy (α). $Co_{1-x}Ni_xCl_2$ alloys were synthesized using CVT growth with the desired stoichiometric ratios of cobalt $(1-x)$ (powder, Alfa-Aesar, 99.99%), nickel (x) (powder, Sigma, 99.99%), and $TeCl_4$ (powder, Sigma, 99.8%) as the transport agent. The overall reaction reads $(1-x)$Co + (x)Ni + (½)$TeCl_4$ = $Co_{1-x}Ni_xCl_2$ + (½)Te where the ½ Te is released as a visibly separated byproduct of the entire reaction.

Stoichiometric amounts of precursors were added to quartz ampoules (15x19x180 mm) and vacuum sealed (~10^{-5} Torr). Considering the hygroscopic nature of $NiCl_2$ and $CoCl_2$ crystals [25], the precursors and ampoules were handled and loaded in a nitrogen-filled glove box before vacuum sealing. Sealed quartz ampoules were heated up in a commercially available three-zone furnace with a temperature gradient of 750° C and 670° C for 72 hours to produce highly crystalline alloys in the cold zone (670° C) with physical sizes reaching more than 1 cm in lateral dimensions as shown in **Fig. 1c**). The designed x values are correlated with the final obtained stoichiometry in our crystals, suggesting 100% of the precursors were involved in the reactions as evidenced by fully alloyed vdW sheets (see **Fig. 1b** and **Appendix B**). This can be attributed to the similar vapor pressure values of Co and Ni and acceptable tolerances of the Hume-Rothery rules. It is noteworthy to mention that starting with Co, Ni, and $TeCl_4$ is critical to obtaining high-quality alloys since the sublimation of stoichiometric amounts of $NiCl_2$ (powder**,** Alfa Aesar**,** 99.5%) and $CoCl_2$ (powder**,** Alfa Aesar**,** 99.5%) usually produced phase-separated crystals and a wide compositional variation within the same crystal.

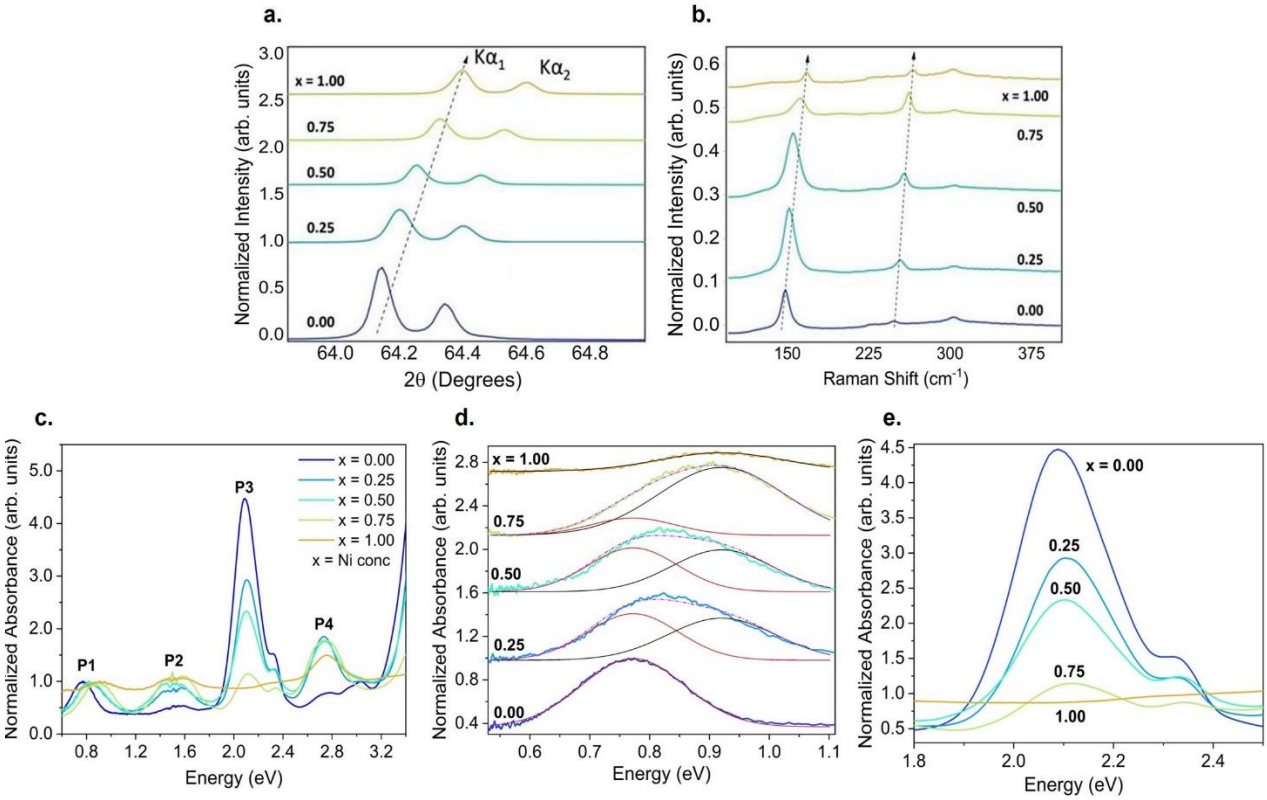

Figure 2: Characterization of $Co_{1-x}Ni_xCl_2$. (**a**) X-Ray diffraction results showing a linear shift in 2θ-d-spacing values as a function of x. (**b**) Raman spectrum. (**c**) UV-Vis absorption spectra for a given compositional value (x) from $x = 0$ (blue) to $x = 1$ (yellow), normalized to the first peak. (**d**) The absorption spectra shows the gradual shift of peak 1 (P1) as x increases from 0 to 1. (**e**) Absorption spectra showing the reduction in absorption intensity of P3 as x increases from 0 to 1. Further experimental details can be found in Appendix A and C.

Our XRD results show that the $Co_{1-x}Ni_xCl_2$ crystals are single-phase without any coexisting phases with XRD (00*l*) peaks (Kα1) gradually shifting from 64.16° to 64.02° with increasing x values from 0 to 1 (**Fig. 2a**). The Raman spectrum (Renishaw micro-Raman with a 488 nm laser source) exhibits two prominent peaks located at 153 cm^{-1} and 248 cm^{-1} for $CoCl_2$ and 171 cm^{-1} and 266 cm^{-1} for $NiCl_2$ (**Fig. 2b**). These modes are associated with in-plane E_g and out-of-plane A_{1g} vibrational modes and both peaks exhibit a very sharp line width (3 cm^{-1}), further demonstrating the high-crystal quality of the synthesized materials [26,27]. As the Ni (x) content is increased, the fundamental vibrational modes (out-of-plane A_{1g} and in-plane E_g) monotonically shift to higher frequencies. This can be attributed to the higher Ni mass and stronger cation-anion bonding. We also note that the reduction in Raman intensity with x might be related to the decreased optical penetration depth. More importantly, the alloyed crystals (**Fig. 2b**) show distinct Raman spectra without any native Raman peak contributions from the parent Ni or Co dihalides. This excludes the possibility of co-existing binary phases.

As the *x* composition is varied in $Co_{1-x}Ni_xCl_2$, the optical properties and the electronic structure show appreciable changes. As shown in **Fig. 2c**, multiple sub-gap absorption peaks (labeled P1 to P4) were identified for the alloy crystals [28,29]. P1 absorption corresponds to the $^4T_1(F) \rightarrow {}^4T_2(F)$ crystal-field transition of $CoCl_2$ and the triplet ground state to spin allowed triplet excited state $^3A_{2g}(F) \rightarrow {}^3T_{2g}(F)$ transition for $NiCl_2$. These two absorption peaks are shifted only by ~0.15 eV. Thus, as the alloying content (x) increases, the P1 peak of Co $^4T_1(F) \rightarrow {}^4T_2(F)$ gradually shifts to the Ni related $^3A_{2g}(F) \rightarrow {}^3T_{2g}(F)$ transition (black curve) in **Fig. 2d**. P2 at 1.5 eV corresponds to the $^4T_1(F) \rightarrow {}^4A_2(F)$ transition of $CoCl_2$ and the $^3A_{2g}(F) \rightarrow {}^3T_{1g}(F)^{(a)}$ electric dipole forbidden transition of $NiCl_2$ (these two nearly appear at the same energies). The P3 peak at 2.1 eV corresponds to the $^4T_1(F) \rightarrow {}^4T_1(P)$ transition of $CoCl_2$, with the small shoulder at 2.4 eV corresponding to the lowest energy spin forbidden $^3A_{2g}(F) \rightarrow {}^1T_{2g}(D)$ transition of $NiCl_2$. Indeed, **Fig. 2e** highlights the sharp decrease in intensity of the 2.1 eV peak for the $CoCl_2$ related $^4T_1(F) \rightarrow {}^4T_1(P)$ transition, as the alloy system becomes increasingly Ni rich. Lastly, the P4 peak at 2.8 eV corresponds to the $^3A_{2g}(F) \rightarrow {}^3T_{1g}(P)^{(b)}$ spin allowed transition of $NiCl_2$ and, as expected, the absorption from this transition gradually increases with x (**Fig. 2c**).

Fig. 3a-c shows the molar susceptibility (χ_m) vs. temperature plots that were obtained from magnetization vs. temperature measurements through a physical property measurement system (PPMS) in VSM mode from 1.7 K to 300 K at $H_{\parallel}$ = 1 T (field applied parallel to the *ab*-plane). As shown in **Fig. 3a**, χ_m for each alloy displays a paramagnetic to antiferromagnetic transition and its first derivative (**Fig. 3a** inset) highlights the corresponding Néel temperature (T_N). The extracted T_N values monotonically increase from 25 to 53 K with increasing Ni content (x), as shown in **Fig. 3c**. The Curie-Weiss Temperature (Θ_W) was extracted using the Curie-Weiss Law, $\chi = \chi_0 + C/(T - \Theta_W)$ (see **Fig. 3b**), where χ_0 is a small diamagnetic background from the sample holder, T is the temperature, and C is the Curie constant. The extracted Θ_W values also show a monotonic increase from 19 K for $x = 0$ to 65 K for $x = 1$.

As shown in **Fig. 3d**, the magnetic saturation (M_s) values depend heavily on the Ni content (x) wherein the M_s observed at ~30 kOe in pure $CoCl_2$ (blue line at $x = 0$) gradually shifts to higher M_s values (light blue and green in **Fig. 3d**) until the M_s value reaches well above 7 Tesla and cannot be observed/measured for compositions $x > 0.75$ (**Fig. 3d**). Here, σ denotes the magnetic

moment per unit mass in units of Am^2/kg. The M-H measurements were performed in $H_{\parallel}$ and $H_{\perp}$ configurations to understand how the magnetic anisotropy evolves for increasing x (**Fig. 3e**). Here, the term α is introduced as a measure of the degree of anisotropy which can be expressed as $\alpha = \frac{|\chi_{\perp} - \chi_{\parallel}|}{\chi_{\perp}}$, where $\chi_{\parallel}$ and $\chi_{\perp}$ are the calculated slopes obtained from the magnetization versus field measurements in $H_{\parallel}$ and $H_{\perp}$ configurations, respectively (**Fig. 3e**). Our results show that α (the degree of magnetic anisotropy) is monotonically reduced for increasing Ni content (x) (**Fig. 3f**). Note that the anisotropy for $x = 1$ remains positive.

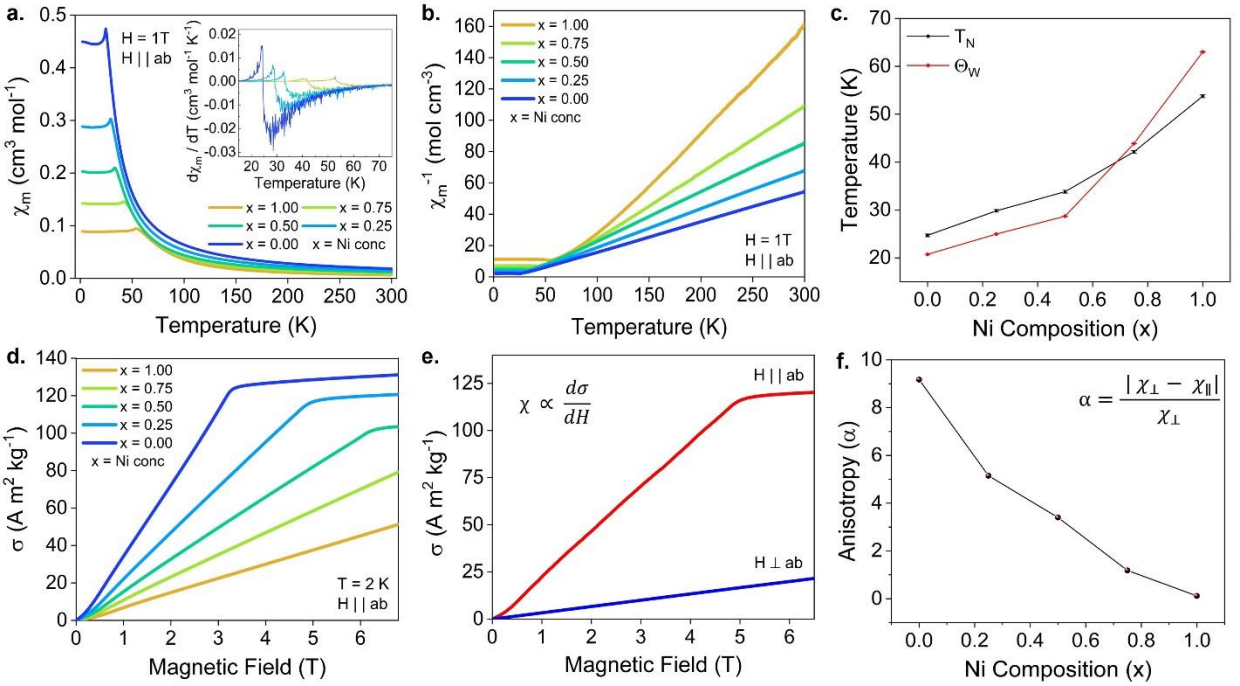

Figure 3: Magnetic characterization of $Co_{1-x}Ni_xCl_2$. (**a**) Susceptibility. (**b**) Inverse susceptibility with respect to temperature for different Ni concentrations (x). (**c**) Extracted Néel temperature and Curie Weiss temperatures for a given composition value (x) in the $H_{\parallel}$ configuration. (**d-f**) In-plane and out-of-plane magnetization vs. field measurements to show how the degree of magnetic anisotropy evolves with increasing Ni concentration. Note that both $CoCl_2$ and $NiCl_2$ have in-plane moments.

We note that alloying has been attempted in other van der Waals magnets such as $RuCl_3$, $M_2P_2S_6$ (M=Fe, Ni, Mn), and Fe_3GeTe_2 [30-34]. As an example, in bulk $(Fe_{1-x}Ni_x)_2P_2S_6$ (x = 0-1) alloys, the symmetry of the structure is also preserved for all x with an antiferromagnetic ground state being similarly obtained for all crystals [31,32]. However, in contrast to $Co_{1-x}Ni_xCl_2$ alloys, $(Fe_{1-x}Ni_x)_2P_2S_6$ offers the possibility of tuning the nature of the magnetic anisotropy upon changing the Ni content ($FePS_3$ has an easy-axis out-of-plane anisotropy whereas $NiPS_3$ has an easy-plane anisotropy instead). In this manner, $(Fe_{1-x}Ni_x)_2P_2S_6$ alloys exhibit a monotonically increasing T_N with increasing nickel content and an easy-axis out-of-plane anisotropy up to $x = 0.9$ (with the degree of anisotropy decreasing with increasing x). For $x > 0.9$, the anisotropy changes to easy-plane, breaking the monotonic T_N trend. The possibility of tuning the nature of the anisotropy of transition metal dihalides upon alloying should be an exciting future direction to pursue when exploring other transition metals (even though both Ni and $CoCl_2$ have in-plane moments, $FeCl_2$ has an out-of-plane easy-axis anisotropy instead [21]).

Next, density functional theory (DFT)-based calculations were performed to offer a detailed understanding of how the magnetic behavior of $Co_{1-x}Ni_xCl_2$ ternary magnets changes with x. First, DFT simulations reveal that for any Ni concentration (x), bulk $Co_{1-x}Ni_xCl_2$ alloys retain an antiferromagnetic insulating magnetic ground state wherein the moments are coupled ferromagnetically (FM) in-plane and antiferromagnetically (AF) out-of-plane. These results are consistent with the experimental results. The derived magnetic moments for Co and Ni are consistent with the expected high-spin state μ_{Co}~2.5 μ_B and μ_{Ni}~1.5 μ_B, reduced with respect to their nominal values due to hybridizations. An orbital moment ~0.1–0.2 μ_B is found in the Co atoms when the spin-orbit coupling is included.

To offer further insights into the magnetic properties of $Co_{1-x}Ni_xCl_2$, we start by building a microscopic model obtained by fitting the energies of different magnetic configurations to a Heisenberg Hamiltonian, where the nearest-neighbor in-plane (J_{intra}) and out-of-plane (J_{inter}) exchange interactions are found to be the dominant couplings (see appendix D for more details). Thus, our effective model Hamiltonian has the form:

$$H = -\frac{J_{intra}}{2}\sum_{[i,j]} \mathbf{S}_i \cdot \mathbf{S}_j - \frac{J_{inter}}{2}\sum_{\langle i,j\rangle} \mathbf{S}_i \cdot \mathbf{S}_j$$

where **S** denotes the spin operators, the summation indices $[i,j]$ ($\langle i,j\rangle$) denote sums over in-plane (out-of-plane) nearest neighbors, and the ½ factor in front of each term is introduced to avoid double-counting.

	BULK			***MONOLAYER***
x	$J_{intra}\mathbf{S}^2$ **(meV)**	$J_{inter}\mathbf{S}^2$ **(meV)**	$E_{\mathbf{MAE}}$ **(meV)**	$J_{intra}\mathbf{S}^2$ **(meV)**
0.00	2.59	-0.43	0.35	2.51
0.25	2.72	-0.44	0.23	2.68
0.50	2.90	-0.44	0.20	2.82
0.75	3.11	-0.45	0.15	3.01
1.00	3.62	-0.45	0.12	3.66

Table 1: Calculated exchange interaction constants for bulk and monolayer $Co_{1-x}Ni_xCl_2$ structures where $0 \leq x \leq 1$. The convention for J is that the coupling parameter is positive for a FM interaction and negative for an AF one. E_{MAE} represents the magnetic anisotropy defined as $E_{\mathrm{G}}(90) - E_{\mathrm{G}}(0)$ where $E_{\mathrm{G}}(\theta)$ is the computed ground state energy as a function of the angle θ that forms the magnetic moment with the atomic planes. $E_{\mathrm{MAE}} > 0$ describes an in-plane anisotropy.

Table 1 shows the evolution of J_{intra} and J_{inter} for the different bulk alloys. As anticipated, J_{intra} is ferromagnetic while J_{inter} is antiferromagnetic in nature. For all x values, the nearest-neighbor ferromagnetic intralayer coupling is the dominant exchange, with the antiferromagnetic interlayer coupling being an order of magnitude smaller. We find that the intralayer exchange (J_{intra}) increases monotonically with the Ni content (x) -from 2.59 meV for $CoCl_2$ to 3.62 meV

for $NiCl_2$. This is a reasonable trend since the magnitude of the exchange is proportional to the degree of orbital overlap, which increases with a decreasing in-plane metal-metal distance (as x increases from 0 to 1). The interlayer exchange, in turn, remains almost unaffected as the interlayer distance does not change significantly enough as to influence the J_{inter}term (from -0.43 meV for $CoCl_2$ to -0.45 meV for $NiCl_2$).

Considering these exchange values and together with a mean-field model, the Néel temperature is proportional to the J values. Considering the calculated variation of $J_{intra}$and J_{inter} with x (**Table 1**), the increase in T_N can be attributed to the increasing J_{intra}value for an increasing Ni content and indicate a good qualitative agreement with the experimentally observed trend in T_N. We note, however, that a mean-field approach-based T_N analysis would yield over-estimates in T_N [35], so we do not proceed further with quantitative evaluations.

Spin-orbit coupling has further been included to obtain an estimate of the magnetic anisotropy energy (MAE) E_{MAE}. Here, $E_{MAE} = E_G(90) - E_G(0)$ where $E_G(\theta)$ is the derived ground state energy as a function of the angle (θ) that forms the magnetic moment with the atomic planes (we have verified that changes in energy for different in-plane magnetization directions are small and pick $M_y = 0$ for the magnetization). **Table 1** shows the derived values for E_{MAE}, where $E_{MAE} > 0$ (describing in-plane moments) and it decreases from $CoCl_2$ to $NiCl_2$, in agreement with experiments (**Fig. 3**).

While experiments are restricted to the bulk, we follow the same theoretical procedure described above to ascertain the magnetic response of $Co_{1-x}Ni_xCl_2$ alloys when going to the strict 2D limit (i.e. down to the monolayer limit). We find that the ground state of the monolayer alloys is ferromagnetic and insulating with the leading exchange interaction term being the nearest neighbor in-plane coupling (J_{intra}), whose calculated values for the different monolayer alloys are shown in **Table 1**. J_{intra} increases monotonically for increasing x with values that are nearly the same as those for the bulk. As mentioned above for the bulk, a mean-field estimate for the transition temperature of the monolayer alloys scales with J_{intra}. Thus, once these exfoliated systems become experimentally feasible, FM monolayers with a Curie temperature that increases with the Ni content can be anticipated.

In conclusion, our experimental and theoretical studies have established metal cation alloying and their magnetic properties in environmentally stable Co and Ni-based $Co_{1-x}Ni_xCl_2$ vdW dihalide magnets. Our results have shown that centimeter-sized $Co_{1-x}Ni_xCl_2$ vdW magnet alloys can be synthesized using the chemical vapor transport technique using elemental precursors from $x = 0$ to 1 without any phase separation. Experimental results have shown that the magnetic anisotropy, Néel temperature, and other magnetic properties can be tuned on-demand with increasing Ni (x) content. Theoretical studies further offered microscopic insights into these magnetic responses through the calculated magnetic exchange interactions. Overall, our results introduce the first metal cation alloying in dihalide magnets and offer new ways to tune the magnetic behavior of these materials on demand.

Acknowledgments

Research supported by the U.S. Department of Energy, Office of Basic Energy Sciences, Division of Materials Sciences and Engineering under Award # SC0020653 (Crystal growth and magnetism), Applied Materials Inc. (crystallography), NSF DMR 1904716 (computational studies), NSF CMMI-1933214 (defect characterization), NSF ECCS 2052527 (electronic characterization), and DMR 2111812 (optical characterization). A.S.B and J. K acknowledge NSF

Grant No. DMR 1904716 (computational efforts) and the ASU Research Computing Center for HPC resources.

Appendix A. Experimental Methods.

Materials characterization. The scanning electron microscopy (SEM) and energy-dispersive X-ray spectroscopy (EDS) mappings were performed using Hitachi S4700 field emission SEM. The working distance and the acceleration voltage was set as 12.9 mm and 15 kV, respectively. The powder X-ray diffraction (XRD) measurements of the as-grown vdW alloys were performed using Cu Kα irradiation on PANalytical X'Pert PRO MRD X-Ray diffraction spectrometer. The Raman spectroscopy was performed under a backscattering geometry using a green laser (λ = 532 nm) as the excitation source with an Andor 750 spectrometer. During the measurements, the incident light and the scattered light were aligned parallel to each other. Magnetic measurements were performed using the physical properties measurement system (PPMS) by Quantum Design Inc. in VSM mode. The specimens were collected in a diamagnetic capsule and measurements were performed from 1.7 K to 300 K from 0 to 7 Tesla magnetic fields. The capsule diamagnetic background correction was done in each measurement set to account for the constant background. The measurements were repeated +20 times on various batches of vdW alloy systems.

Appendix B. Energy Dispersive X-Ray Spectra

In **Fig. 1b** we have shown the SEM/EDS images and maps for $Co_{1-x}Ni_xCl_2$ wherein $x = 0.25$. Here, we present the SEM/EDS images and maps for the whole alloy system from $x = 0$ to $x = 1$ (**Figs. 4-8**, respectively). This confirms the stoichiometry of the crystals and highlights that the crystals are Te free.

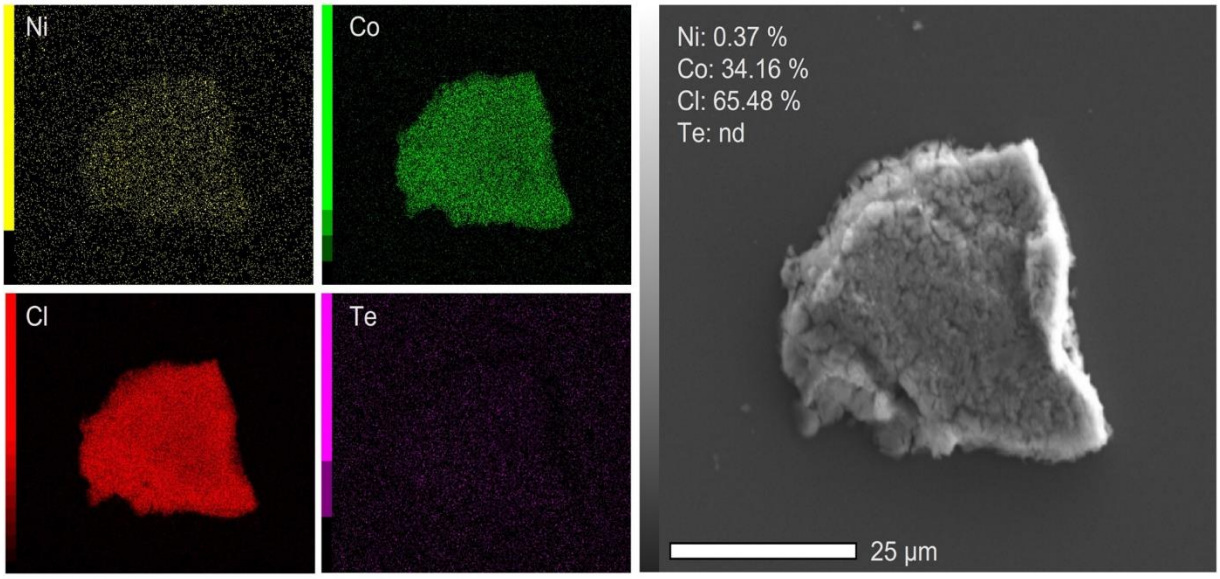

Figure 4: SEM/EDS images for $CoCl_2$.

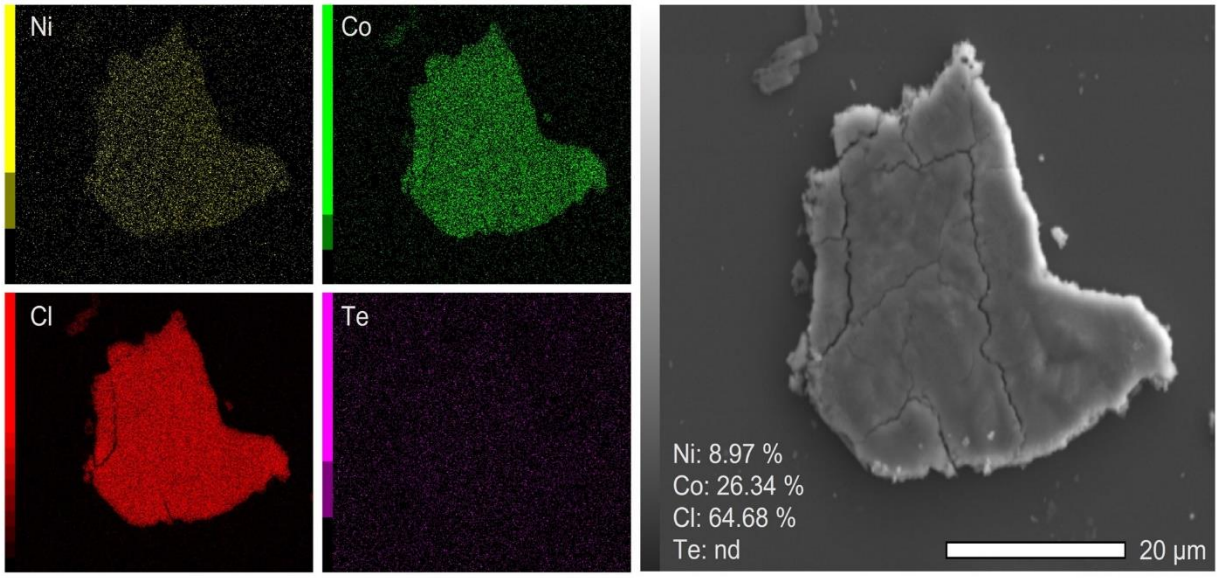

Figure 5: SEM/EDS images for $Co_{0.75}Ni_{0.25}Cl_2$.

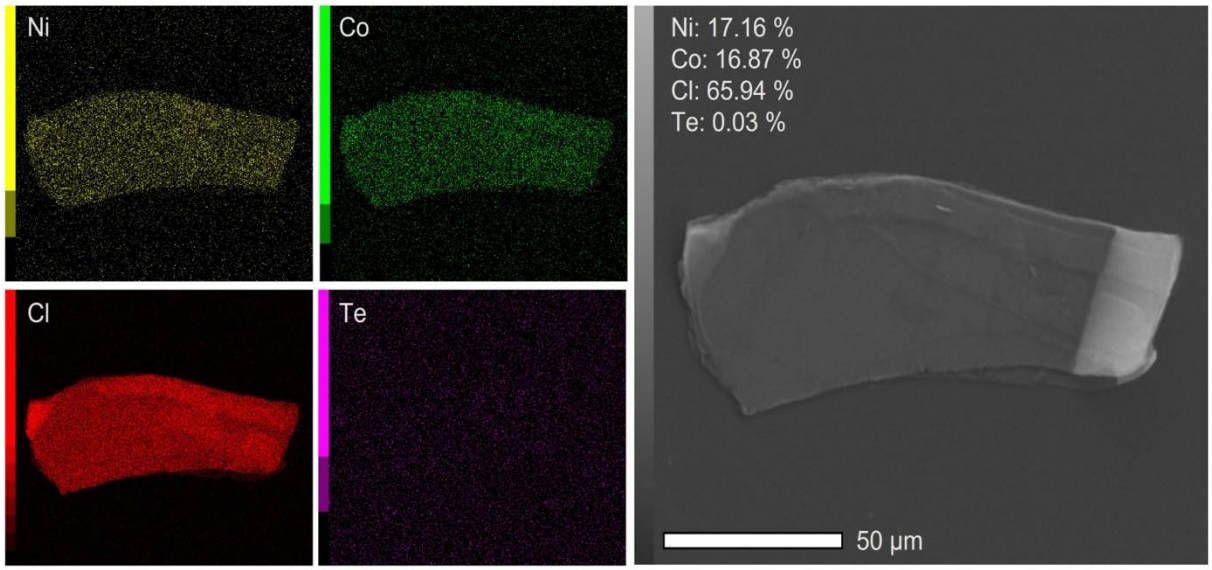

Figure 6: SEM/EDS images for $Co_{0.5}Ni_{0.5}Cl_2$.

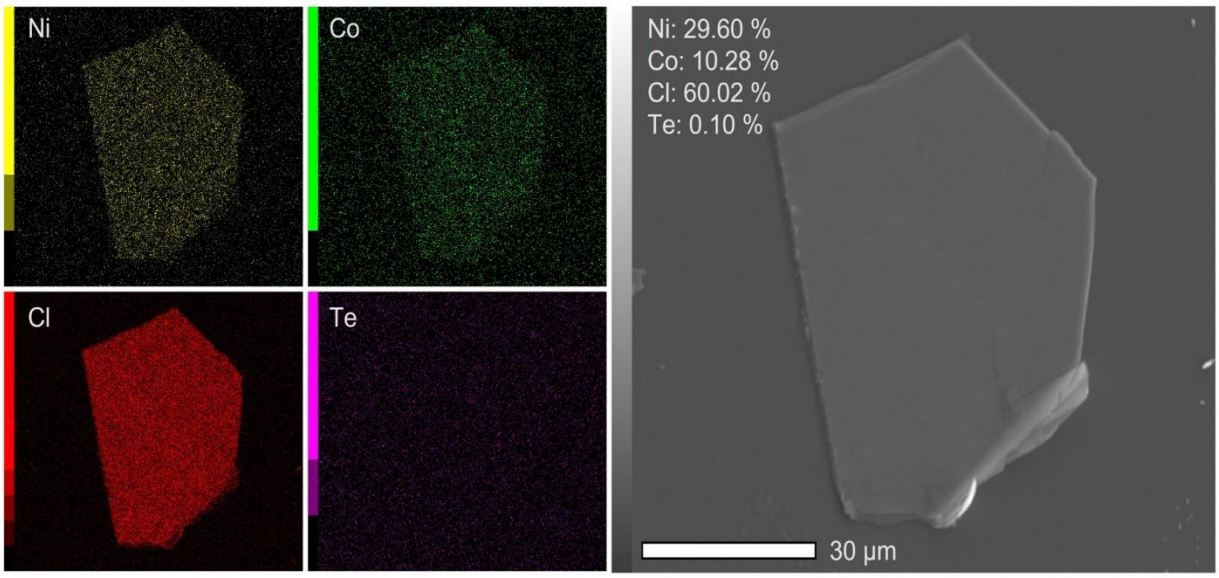

Figure 7: SEM/EDS images for $Co_{0.25}Ni_{0.75}Cl_2$.

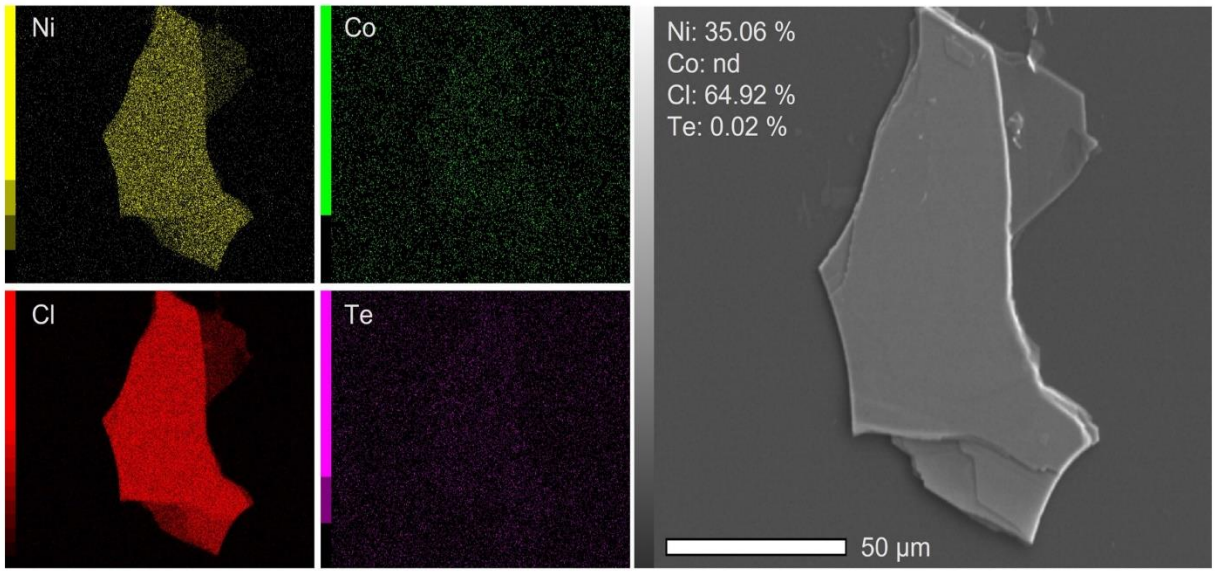

Figure 8: SEM/EDS images for $NiCl_2$.

Appendix C. Powder XRD of $NiCl_2$

In **Fig. 2a** we have shown the linear shift of 2Θ values as a function of x. Here, we present the full powder XRD spectra of $NiCl_2$ (see **Fig. 9**) to highlight the high quality of the synthesized crystals.

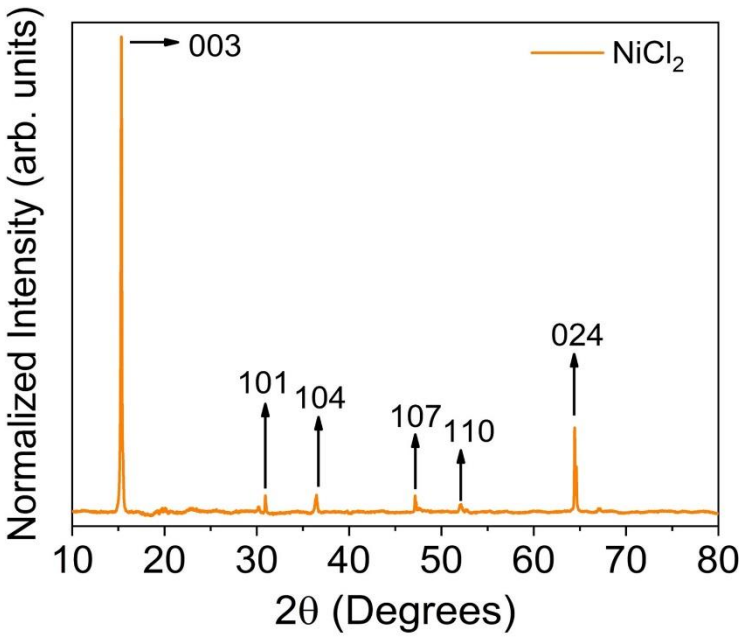

Figure 9: Powder XRD spectra of $NiCl_2$.

Appendix D. First-principles calculations.

Computational Methods: DFT calculations for $Co_{1-x}Ni_xCl_2$ alloys were performed with the all-electron, full potential code WIEN2k [36] based on the augmented plane wave plus local orbitals (APW+lo) basis set. We used the Perdew-Burke-Ernzerhof (PBE) version of the generalized-gradient approximation [37] (GGA) as the exchange-correlation functional. All calculations were converged with respect to $R_{\mathrm{mt}}K_{\mathrm{max}} = 7.0$ and the number of k-points, where the following k-mesh sizes were used in sampling over the Brillouin zones of the bulk (monolayer) cells: 26x26x14 (41x41x5) for $x = 0$ and $x = 1$, 21x21x22 (33x33x8) for $x = 0.25$ and $x = 0.75$, and 17x18x30 (7x27x48) for $x = 0.5$. The muffin-tin radii used were 2.46 Å for Co, 2.43 Å for Ni, and 2.10 Å for Cl. The spin-orbit interaction was considered using a second variational method with scalar-relative orbitals as basis states [36]. We did not add an on-site Coulomb repulsion (U) since insulating solutions can already be obtained at the GGA level and, in this manner, the derived exchange constants are not dependent on the chosen value of U.

Structural data: As a starting point we used bulk experimental structural data [22] for $CoCl_2$ and $NiCl_2$. The bulk $Co_{1-x}Ni_xCl_2$ alloy ($x = 0.25$, 0.50, and 0.75) unit cells were then constructed from a 2x2x1 supercell of the experimental one. Ideally, larger supercells should be attempted for alloys, but given the clean trends found experimentally and in our calculations for the J/T_{N} dependence, we used a minimal model that is able to reproduce experimental trends.

Structural relaxations (lattice parameters and atomic coordinates) were performed in the magnetic ground state (AF for the bulk) using the GGA-PBE functional and the computational parameters mentioned above, as well as with a force convergence criterion of 0.5 mRy/bohr. The optimized bulk interlayer distances (d) and in-plane lattice parameters (a) were found to be consistent with experimentally reported values for $CoCl_2$ and $NiCl_2$ [20-22], and the latter were found to decrease monotonically with increasing x, as expected (see **Table 2** for bulk optimized cell parameters and bond-lengths). For the monolayer structures, in-plane lattice parameters were taken from the optimized bulk structures and the internal coordinates were further relaxed with FM order and the same force convergence value as the bulk (see **Table 2** for monolayer optimized bond-lengths). Also, a vacuum level of ~23 Å was used to ensure no out-of-plane interactions.

	BULK					**MONOLAYER**	
x	a **(Å)**	c **(Å)**	d **(Å)**	**Co-Cl (Å)**	**Ni-Cl (Å)**	**Co-Cl (Å)**	**Ni-Cl (Å)**
0.00	3.55	11.63	5.81	2.44	-	2.45	-
0.25	3.54	11.60	5.80	2.44	2.41	2.45	2.42
0.50	3.53	11.54	5.77	2.43	2.41	2.44	2.41
0.75	3.52	11.61	5.80	2.43	2.41	2.44	2.41
1.00	3.50	11.58	5.79	-	2.41	-	2.41

Table 2: In-plane lattice parameter (a), out-of-plane lattice parameter (c), interlayer distance (d), and Co-Cl/Ni-Cl bond lengths for the $Co_{1-x}Ni_xCl_2$ DFT-relaxed bulk and monolayer structures.

Energy Fittings to Heisenberg Hamiltonian: As mentioned in the main text, we extract the leading magnetic couplings by fitting the energy differences of different magnetic configurations to a Heisenberg model. We describe here the magnetic configurations we used for the energy fittings at the bulk and monolayer levels. In the bulk $Co_{1-x}Ni_xCl_2$ structures, each transition-metal atom has six in-plane nearest-neighbors and two out-of-plane nearest neighbors (the latter corresponding to next-nearest neighbors). We used the following magnetic configurations: 1) ferromagnetic (FM) configuration wherein the in-plane and out-of-plane nearest neighbor spins are FM-aligned (corresponding to $E_{FM} = E_0 - (6J_{intra} + 2J_{inter})\mathbf{S}^2$). 2) Antiferromagnetic (AF) configuration wherein in-plane nearest neighbors are FM coupled in-plane and AF out-of-plane (corresponding to $E_{AF} = E_0 - (6J_{intra} - 2J_{inter})\mathbf{S}^2$). 3) An antiferromagnetic striped configuration (AFS) in which each transition metal atom has two in-plane nearest neighbors with parallel spins and four with anti-parallel spins (corresponding to $E_{AFS} = E_0 + (2J_{intra} - 2J_{inter})\mathbf{S}^2$. Note that in each of the expressions above, the energy maps correspond to one formula unit. Using these energy configurations, we can solve for J_{intra} and J_{inter} in terms of the energy differences $J_{intra} = \frac{1}{8\mathbf{S}^2}[(E_{AFS} - E_{AF}) - (E_{FM} - E_{AF})]$, and $J_{inter} = -\frac{1}{4\mathbf{S}^2}(E_{FM} - E_{AF})$. The bulk values for J_{intra} and J_{inter} in **Table 1** of the main text are obtained using this methodology. In the case of the monolayer $Co_{1-x}Ni_xCl_2$ structures, we use the same energy fittings for E_{FM} and E_{AFS} as for the bulk, which allows us to obtain $J_{intra}^{mono} = \frac{1}{8\mathbf{S}^2}(E_{AFS} - E_{FM})$.

References

[1] J.-U. Lee, S. Lee, J. H. Ryoo, S. Kang, T. Y. Kim, P. Kim, C.-H. Park, J.-G. Park, and H. Cheong, Ising-Type Magnetic Ordering in Atomically Thin $FePS_3$, Nano Lett. **16**, 743 (2016).

[2] B. Huang, G. Clark, E. Navarro-Moratalla, D. R. Klein, R. Cheng, K. L. Seyler, D. Zhong, E. Schmidgall, M. A. McGuire, D. H. Cobden, W. Yao, D. Xiao, P. Jarillo-Herrero, and X. Xu, Layer-dependent ferromagnetism in a van der Waals crystal down to the monolayer limit, Nature **546**, 270 (2017).

[3] A. Bedoya-Pinto, J.-R. Ji, A. K. Pandeya, P. Gargiani, M. Valvidares, P. Sessi, J. M. Taylor, F. Radu, K. Chang, and S. S. P. Parkin, Intrinsic 2D-XY ferromagnetism in a van der Waals monolayer, Science **374**, 616 (2021).

[4] C. Gong, L. Li, Z. Li, H. Ji, A. Stern, Y. Xia, T. Cao, W. Bao, C. Wang, Y. Wang, Z. Q. Qiu, R. J. Cava, S. G. Louie, J. Xia, and X. Zhang, Discovery of intrinsic ferromagnetism in two-dimensional van der Waals crystals, Nature 546, 265 (2017).

[5] Y. Deng, Y. Yu, Y. Song, J. Zhang, N. Z. Wang, Z. Sun, Y. Yi, Y. Z. Wu, S. Wu, J. Zhu, J. Wang, X. H. Chen, and Y. Zhang, Gate-tunable room-temperature ferromagnetism in two-dimensional Fe_3GeTe_2, Nature **563**, 94 (2018).

[6] D. Amoroso, P. Barone, and S. Picozzi, Spontaneous skyrmionic lattice from anisotropic symmetric exchange in a Ni-halide monolayer, Nature Comm. **11**, 5784 (2020).

[7] A. S. Botana and M. R. Norman, Electronic structure and magnetism of transition metal dihalides: Bulk to monolayer, Phys. Rev. Mater. **3**, 044001 (2019).

[8] K. S. Burch, D. Mandrus, and J.-G. Park, Magnetism in two-dimensional van der Waals materials, Nature **563**, 47 (2018).

[9] T. Kong, S. Guo, D. Ni, and R. J. Cava, Crystal structure and magnetic properties of the layered van der Waals compound VBr_3, Phys. Rev. Mater. **3**, 084419 (2019).

[10] J. L. Lado and J. Fernández-Rossier, On the origin of magnetic anisotropy in two dimensional CrI_3, 2D Mater. **4**, 035002 (2017).

[11] M. A. McGuire, J. Yan, P. Lampen-Kelley, A. F. May, V. R. Cooper, L. Lindsay, A. Puretzky, L. Liang, S. KC, E. Cakmak, S. Calder, and B. C. Sales, High-temperature magnetostructural transition in van der Waals-layered α−$MoCl_3$, Phys. Rev. Mater. **1**, 064001 (2017).

[12] M. Gibertini, M. Koperski, A. F. Morpurgo, and K. S. Novoselov, Magnetic 2D materials and heterostructures, Nature Nanotechnol. **14**, 408 (2019).

[13] M. Blei, J. L. Lado, Q. Song, D. Dey, O. Erten, V. Pardo, R. Comin, S. Tongay, and A. S. Botana, Synthesis, engineering, and theory of 2D van der Waals magnets, Appl. Phys. Rev. **8**, 021301 (2021).

[14] Q. Wang, N. Han, X. Zhang, C. Zhang, X. Zhang, and Y. Chen, Modulation of electronic and magnetic properties of monolayer chromium trihalides by alloy and strain engineering, J. Appl. Phys. **129**, 155104 (2021).

[15] M. Abramchuk, S. Jaszewski, K. R. Metz, G. B. Osterhoudt, Y. Wang, K. S. Burch, and F. Tafti, Controlling Magnetic and Optical Properties of the van der Waals Crystal $CrCl_{3-x}Br_x$ via Mixed Halide Chemistry, Adv. Mater. **30**, 1801325 (2018).

[16] T. A. Tartaglia, J. N. Tang, J. L. Lado, F. Bahrami, M. Abramchuk, G. T. McCandless, M. C. Doyle, K. S. Burch, Y. Ran, J. Y. Chan, and F. Tafti, Accessing new magnetic regimes by tuning the ligand spin-orbit coupling in van der Waals magnets, Sci. Adv. **6**, eabb9379 (2020).

[17] X. Li, Z. Zhang, and H. Zhang, High throughput study on magnetic ground states with Hubbard U corrections in transition metal dihalide monolayers, Nanoscale Adv. **2**, 495 (2020).
[18] V. V. Kulish and W. Huang, Single-layer metal halides MX2 (X = Cl, Br, I): stability and tunable magnetism from first principles and Monte Carlo simulations, J. Mater. Chem. C **5**, 8734 (2017).
[19] H. Grime and J. A. Santos, The Structure and Colour of Anhydrous Cobalt Chloride, $CoCl_2$, at Room and very Low Temperatures, Zeitschrift für Kristallographie - Crystalline Materials **88**, 136 (1934).
[20] A. Ferrari, A. Braibanti, and G. Bigliardi, Refinement of the crystal structure of NiCl2 and of unit-cell parameters of some anhydrous chlorides of divalent metals, Acta Crystallographica **16**, 846 (1963).
[21] M. A. McGuire, Crystal and Magnetic Structures in Layered, Transition Metal Dihalides and Trihalides, Crystals **7**, 121 (2017).
[22] M. K. Wilkinson, J. W. Cable, E. O. Wollan, and W. C. Koehler, Neutron Diffraction Investigations of the Magnetic Ordering in $FeBr_2$, $CoBr_2$, $FeCl_2$, and $CoCl_2$, Phys. Rev. **113**, 497 (1959).
[23] R. H. Busey and W. F. Giauque, The Heat Capacity of Anhydrous $NiCl_2$ from 15 to 300°K. The Antiferromagnetic Anomaly near 52°K. Entropy and Free Energy, J. Am. Chem. Soc. **74**, 4443 (1952).
[24] R. J. Pollard, V. H. McCann, and J. B. Ward, Electronic and magnetic properties of ^{57}Fe in $NiCl_2$, $NiBr_2$, NiI_2 and CoI_2 from Mossbauer spectroscopy, J. Phys. C: Solid State Phys. **15**, 6807 (1982).
[25] C. Starr, F. Bitter, and A. R. Kaufmann, The Magnetic Properties of the Iron Group Anhydrous Chlorides at Low Temperatures. I. Experimental, Phys. Rev. **58**, 977 (1940).
[26] D. J. Lockwood, Lattice vibrations of $CdCl_2$, $CdBr_2$, $MnCl_2$, and $CoCl_2$: infrared and Raman spectra, J. Opt. Soc. Am. **63**, 374 (1973).
[27] D. J. Lockwood, D. Bertrand, P. Carrara, G. Mischler, D. Billerey, and C. Terrier, Raman spectrum of $NiCl_2$, J. Phys. C: Solid State Phys. **12**, 3615 (1979).
[28] M. Kozielski, I. Pollini, and G. Spinolo, Electronic absorption spectra of Ni^{2+} in $NiCl_2$ and $NiBr_2$. (Phonon and magnon sidebands), J. Phys. C: Solid State Phys. **5**, 1253 (1972).
[29] I. Hernández and F. Rodríguez, On the pressure-induced spin transition in $CoCl_2$. Interplay between Jahn-Teller effect and spin sate in Co^{2+}, J. Phys.: Conf. Ser. **121**, 042006 (2008).
[30] M. Roslova, J. Hunger, G. Bastien, D. Pohl, H. M. Haghighi, A. U. B. Wolter, A. Isaeva, U. Schwarz, B. Rellinghaus, K. Nielsch, B. Büchner, and T. Doert, Detuning the Honeycomb of the α-$RuCl_3$ Kitaev Lattice: A Case of Cr^{3+} Dopant, Inorg. Chem. **58**, 6659 (2019).
[31] S. Selter, Y. Shemerliuk, M.-I. Sturza, A. U. B. Wolter, B. Büchner, and S. Aswartham, Crystal growth and anisotropic magnetic properties of quasi-two-dimensional $(Fe_{1-x}Ni_x)_2P_2S_6$, Phys. Rev. Mat. **5**, 073401 (2021).
[32] S. Lee, J. Park, Y. Choi, K. Raju, W.-T. Chen, R. Sankar, and K.-Y. Choi, Chemical tuning of magnetic anisotropy and correlations in $Ni_{1-x}Fe_xPS_3$, Phys. Rev. B **104**, 174412 (2021).
[33] G. Drachuk, Z. Salman, M. W. Masters, V. Taufour, T. N. Lamichhane, Q. Lin, W. E. Straszheim, S. L. Bud'ko, and P. C. Canfield, Effect of nickel substitution on magnetism in the layered van der Waals ferromagnet Fe_3GeTe_2, Phys. Rev. B **98**, 144434 (2018).

[34] Y. Shemerliuk, Y. Zhou, Z. Yang, G. Cao, A. U. B. Wolter, B. Büchner, and S. Aswartham, Tuning Magnetic and Transport Properties in Quasi-2D $(Mn_{1-x}Ni_x)_2P_2S_6$ Single Crystals, Electron. Mater. **2**, 284 (2021).
[35] N. W. Ashcroft and N. D. Mermin, Solid State Physics, New York: Holt, Rinehart and Winston (1976).
[36] An augmented plane wave plus local orbitals program for calculating crystal properties: Wien2K User's Guide, Techn. Universitat Wien, (2008).
[37] J. P. Perdew, K. Burke, and M. Ernzerhof, Generalized Gradient Approximation Made Simple, Phys. Rev. Lett. **77**, 3865 (1996).